Numerical Investigations of the Hydrodynamics of an Oscillating Water Column Device

Arun Kamath[1], Hans Bihs, Øivind A. Arntsen

Department of Civil and Transport Engineering, Norwegian University of Science and Technology, 7491 Trondheim, Norway

Abstract

An Oscillating Water Column (OWC) device is a renewable energy device that is used to extract ocean wave energy through the action of waves on a partially submerged chamber consisting of an air and a water column. The operation of an OWC device involves complex hydrodynamic interactions between the waves and the device and a good understanding of these interactions is essential for the design of hydrodynamically efficient and structurally stable devices.

In this paper, a two-dimensional numerical wave tank is utilized to simulate the interaction of an OWC device with waves of different wavelengths and steepnesses. The chamber pressure, provided by a turbine in a prototype, is simulated using porous media flow theory in the numerical model. The pressure in the chamber and the velocity of the free surface is calculated to evaluate the efficiency of the device and the model is validated by comparing the numerical results with experimental data. The performance of the device under a range of wavelengths for different wave steepnesses is evaluated. The effect of wave steepness on the device efficiency at a lower wave steepness was found to be low, but a large reduction in performance was found in the presence of steep non-linear waves.

Keywords: Oscillating Water Column, Computational Fluid Dynamics, wave

[1]Corresponding Author, Email: arun.kamath@ntnu.no, Ph: (+47) 73 59 46 40, Fax: (+47) 73 59 70 21

energy, porous media, REEF3D

1. Introduction

An Oscillating Water Column (OWC) device is a renewable energy device that is used to capture ocean wave energy and convert it to electrical energy. An OWC device consists of a chamber that is partially submerged in water and has an air column trapped above the water column. The water column in the chamber is excited by the incoming waves and the motion of the water column is transferred to the air column which is forced through a vent at the roof of the chamber. The pressurised air flows through the vent and drives a turbine to generate electrical energy. A good understanding of the hydrodynamics around an OWC device is essential in order to efficiently harness wave energy and to develop stable and economical OWC devices.

Several researchers have mathematically analyzed the hydrodynamics of an OWC device and devised formulae to evaluate the hydrodynamic efficiency. Evans (1978) calculated the efficiency of a wave energy converter modeled as a pair of parallel vertical plates, with a float connected to a spring-dashpot on the free surface as the wave energy absorber. This model considered the length of the chamber to be small compared to the waves and the water column moves like a weightless piston, resulting in a one-dimensional rigid motion of the free surface. Evans (1982) further studied the OWC device, including the spatial variation of the free surface and related the hydrodynamics to the dynamic air pressure developed in the chamber. This is considered to be a better representation of the system, as the free surface motion does not need to be piston-like under all operating conditions. Sarmento and Falcão (1985) developed a theory to evaluate the hydrodynamic efficiency of an OWC device with both linear and non-linear power take-off (PTO) systems. The authors concluded that the non-linear PTO was only marginally lower in efficiency compared to the linear system. They also noted that the device efficiency could be improved by introducing phase control, where the volume flow of air is controlled independently of the pressure by varying the external damping on the chamber. Sarmento (1992) carried out wave flume experiments of an OWC device using a small amplitude-to-wavelength ratio, A_0/λ and validated the theory presented by Sarmento and Falcão (1985). The external damping from a power take-off device was modeled using porous filter material and orifice plates to represent linear and non-linear PTO mechanisms respectively. The importance of external damping was presented by Thiruvenkatasamy and Neelamani (1997), who studied the effect of the nozzle area on the efficiency of an OWC device through wave flume experiments. In their experiments, the air pressure in the chamber was lowered for nozzle cross-sectional areas greater than 0.81% of the free surface, resulting in a lower device efficiency. This implies that an optimal damping on the chamber is required under prevalent wave conditions in order to efficiently extract the incident wave energy. Morris-Thomas et al. (2007) carried out experiments to determine the influence of wall thickness, shape of the front wall and the draught of the front wall for various wave parameters on the hydrodynamic efficiency of an OWC device. They reported a peak efficiency of about 0.7 and that the shape parameters of the device affect the bandwidth of the hydrodynamic efficiency curve. They concluded that a hydrodynamically smooth front wall slightly reduced the entrance losses, resulting in a slightly larger amount of wave energy available in the device chamber. Zhang et al. (2012) simulated the experiments presented by Morris-Thomas et al. (2007) with a two-dimensional Computational Fluid Dynamics (CFD) based numerical model and presented the variation of the pressure and the free surface elevation inside the chamber, however without comparison to the experimental data. They reported reasonable agreement with experimental data for the hydrodynamic efficiency of the device with a slight over prediction of the efficiency in the model due to the complex pressure changes in the chamber around resonance. Teixeira et al. (2013) used a numerical model based on the semi-implicit Taylor-Galerkin method to simulate regular wave interaction with an OWC device including the aerodynamics in the chamber using the first law of thermodynamics and ideal gas transformation and compared their results with numerical results from the commercial CFD code Fluent. López et al. (2014) validated a CFD model using experimental results and studied the importance of external damping on the performance of an OWC device under regular and irregular waves to determine the optimum turbine-induced damping on an OWC device.

The OWC device absorbs wave energy through the motion of the air column that is pressurized due to the damping provided by the air vent and the power take-off device. This external damping on the device chamber is represented by a nozzle or vent in the roof of the chamber in experimental studies by Thiruvenkatasamy and Neelamani (1997) and Morris-Thomas et al. (2007). Sarmento (1992) used orifice plates and porous filter material. The use of a porous filter material in model testing is one of the methods to represent a linear power take-off device. This is justified by the fact that a Wells turbine is approximately linear and this simple method provides a good representation of the linear pressure-versus-flow rate characteristics (Falcão and Henriques, 2014). In a numerical model, the effect of a power take-off device can be simulated by considering the air flow in the vent as a flow through a porous medium. In the case of a linear power take-off device, the pressure drop across the vent due the presence of the porous medium can be governed by a linear pressure drop law. It is also possible to numerically implement a quadratic pressure drop law to simulate the effect of a self-rectifying impulse turbine. This method provides a good representation of the external damping on the device chamber to study the device hydrodynamics without difficulties in numerical computations due to the high air velocities in an air vent of a small width.

In current literature, there are not many numerical studies which control external damping in an explicit manner without changing the size of the air vent. Didier et al. (2011) used porous media theory to define external damping on an OWC device modeled as a cylinder of small diameter. The application of the porous media flow theory to model the pressure drop across the vent on model scale OWC devices would help in understanding the hydrodynamics of the device in combination with the effect from the PTO device. The use of porous media flow theory to model the external damping provides the means to control the variation of the chamber pressure. The control over the chamber pressure variation is part of a strategy to improve the performance of the device, called phase control. This concept has been presented by several authors, for example Hoskin et al. (1986), Falcão and Justino (1999) and Lopes et al. (2009). A combined approach to model the variation of the free surface and the chamber pressure and control the pressure drop across the vent in the numerical model will provide useful insights into the operation of the device.

The objective of this study is to investigate the hydrodynamics of an OWC device including the variation of the free surface and pressure inside the chamber and represent the external damping provided by the PTO device using the porous media flow theory. The study uses a CFD model to carry out two-dimensional simulations of an OWC device placed in a numerical wave tank. The experimental data from Morris-Thomas et al. (2007) is used to validate the numerical model. The pressure drop in the experiments is quantified using the porous media flow theory and the external damping on the chamber is defined independent of the air vent width in the numerical model. The numerical model assumes incompressible air in the device chamber because the effect of air compressibility is negligible in the small scale model considered in this study as the ratio between the chamber volume and the OWC free surface is relatively small and much smaller than in a full-scale prototype. The variation of the free surface, chamber pressure and the velocity of the vertical free surface motion in the numerical model are compared to the experimental observations. The efficiency of the device over a range of wavelengths is calculated for a fixed wave amplitude. In real sea states, the incident wave amplitude may change over time. In order to investigate the performance of the device under changing conditions in the sea states, the effect of wave steepness on the device efficiency and performance under steep non-linear waves is evaluated. The knowledge gained from these studies using regular waves can help in obtaining a better understanding of the device performance under different wave steepnesses and amplitudes that are encountered in real sea states.

2. Numerical Model

The open-source CFD model REEF3D solves the fluid flow problem using the incompressible Reynolds-averaged Navier-Stokes (RANS) equations along with the continuity equation:

$$\frac{\partial U_i}{\partial x_i} = 0 \tag{1}$$

$$\frac{\partial U_i}{\partial t} + U_j \frac{\partial U_i}{\partial x_j} = -\frac{1}{\rho}\frac{\partial P}{\partial x_i} + \frac{\partial}{\partial x_j}\left[(\nu + \nu_t)\left(\frac{\partial U_i}{\partial x_j} + \frac{\partial U_j}{\partial x_i}\right)\right] + g_i \tag{2}$$

where U is the velocity averaged over time t, ρ is the fluid density, P is the pressure, ν is the kinematic viscosity, ν_t is the eddy viscosity and g is the acceleration due to gravity.

Chorin's projection method (Chorin, 1968) is used to determine the pressure and a preconditioned BiCGStab solver (van der Vorst, 1992) is used to solve the resulting Poisson pressure equation. Turbulence modeling is handled using the two-equation k-ω model proposed by Wilcox (1994), where the transport equations for the turbulent kinetic energy, k and the specific turbulent dissipation rate, ω are:

$$\frac{\partial k}{\partial t} + U_j \frac{\partial k}{\partial x_j} = \frac{\partial}{\partial x_j}\left[\left(\nu + \frac{\nu_t}{\sigma_k}\right)\frac{\partial k}{\partial x_j}\right] + P_k - \beta_k k\omega \tag{3}$$

$$\frac{\partial \omega}{\partial t} + U_j \frac{\partial \omega}{\partial x_j} = \frac{\partial}{\partial x_j}\left[\left(\nu + \frac{\nu_t}{\sigma_\omega}\right)\frac{\partial \omega}{\partial x_j}\right] + \frac{\omega}{k}\alpha P_k - \beta\omega^2 \tag{4}$$

$$\nu_t = \frac{k}{\omega} \tag{5}$$

where, P_k is the production rate and closure coefficients $\sigma_k = 2$, $\sigma_\omega = 2$, $\alpha = 5/9$, $\beta_k = 9/100$, $\beta = 3/40$.

The highly strained flow due to the waves results in an overproduction of turbulence in the numerical wave tank. This is avoided by modifying the eddy viscosity formulation to introduce a stress limiter formula based on the Bradshaw et al. (1967) assumption as shown by Durbin (2009):

$$\nu_t \leq \sqrt{\frac{2}{3}} \frac{k}{|\mathbf{S}|} \tag{6}$$

where $\mathbf{S}$ stands for the source terms in transport equations. The large difference between the density of air and water leads to a large strain at the interface in a two-phase CFD model. In reality, the free surface is a boundary at which eddy viscosity damping occurs. This effect is not accounted for in the $k - \omega$ model. The overproduction of turbulence due to the additional strain in this case is reduced using free surface turbulence damping using a source term in the specific turbulent dissipation equation as shown by Egorov (2004):

$$S_n = \left(\frac{6 \ B \ \nu}{\beta \ dx^2} \right)^2 \beta \ dx \ \delta \left(\phi \right) \tag{7}$$

where, model parameter B is set to 100.0 and dx is the grid size. The Dirac delta function, $\delta(\phi)$ is used to apply the limiter only at the free surface.

The fifth-order conservative finite difference Weighted Essentially Non-Oscillatory (WENO) scheme proposed by Jiang and Shu (1996) is used for the discretization of the convective terms of the RANS equations. The Hamilton-Jacobi formulation of the WENO scheme (Jiang and Peng, 2000) is used to discretize the level set function ϕ, turbulent kinetic energy k and the specific turbulent dissipation rate ω. The WENO scheme provides the accuracy required to model complex free surface flows and is a minimum third-order accurate in the presence of large gradients and shocks. A Total Variation Diminishing (TVD) third-order Runge-Kutta explicit time scheme by Shu and Osher (1988) is employed for the time treatment of the momentum equation, the level set function and the reinitialisation equation. An adaptive time stepping strategy is employed in the model to determine the time step size in the simulation using the Courant-Frederick-Lewis (CFL) criterion. The time advancement of k, and ω is carried out with a first-order implicit scheme. These variables are largely driven by source terms and have a low influence from the convective terms. An explicit treatment of these variables would result in very small time steps due to the large source terms and this is avoided by the implicit treatment of the variables. In addition, the diffusion terms of the velocities are also handled using an implicit scheme, removing them from the CFL criterion.

The model uses a Cartesian grid for spatial discretization, which facilitates a straight forward implementation of the finite difference schemes. The boundary conditions for complex geometries are handled using an adaptation of the Immersed Boundary Method (IBM), where the values from the fluid region are extrapolated into the solid region using ghost cells (Berthelsen and Faltinsen, 2008). The computational performance of the model is improved using the MPI library. The domain is decomposed into smaller parts and a processor is assigned to each part. The numerical model is completely parallelised and can be executed on high performance computing systems.

2.1. Level Set Method

The free surface is obtained using the level set method. In this method, the zero level set of a signed distance function, $\phi(\vec{x},t)$ called the level set function, represents the interface between water and air. For the rest of the domain, the level set function represents the closest distance of each point in the domain from the interface and the sign distinguishes the two fluids across the interface. The level set function is defined as:

$$\phi(\vec{x},t)\begin{cases} >0 & if\ \vec{x}\ is\ in\ phase\ 1 \\ =0 & if\ \vec{x}\ is\ at\ the\ interface \\ <0 & if\ \vec{x}\ is\ in\ phase\ 2 \end{cases} \tag{8}$$

The level set function is smooth across the interface and provides a sharp description of the free surface. The signed distance property of the level set function is lost when the interface moves. A partial differential equation based reinitialisation procedure presented by Peng et al. (1999) is then used to restore the signed distance property of the function.

2.2. Numerical Wave Tank

In a two dimensional numerical wave tank, symmetry conditions are enforced on the side walls and the top of the tank. The bottom wall of the tank and boundaries of objects placed in the tank are treated with a no-slip or wall boundary condition. A relaxation method is used for wave generation and absorption. In this method, an analytical solution obtained from wave theory is used to moderate the computational values in the relaxation zones. Implementation of the relaxation method has been demonstrated by Mayer et al. (1998), Engsig-Karup (2006) and Jacobsen et al. (2011). The values of the velocity and the free surface are moderated in the relaxation zones for wave generation and absorption zones using the following equations:

$$\begin{aligned} U_{relaxed} &= \Gamma(x) U_{analytical} + (1 - \Gamma(x)) U_{computational} \\ \phi_{relaxed} &= \Gamma(x) \phi_{analytical} + (1 - \Gamma(x)) \phi_{computational} \end{aligned} \tag{9}$$

where $\Gamma(x)$ is called the relaxation function and $x \in [0, 1]$ is the length scale along the relaxation zone.

The relaxation function is a smooth function with a range $[0, 1]$ and it facilitates the smooth transition between the computational and analytical values in the relaxation zones. In this study, the set of relaxation functions presented by Engsig-Karup (2006) for wave generation and absorption is used, where three relaxation zones are defined in the numerical wave tank. First, in the wave generation zone, the computational values of velocity and free surface are taken from zero to the analytical values expected using the appropriate wave theory using Eq. (9). The relaxation function transitions the values of velocity and free surface to the values prescribed by the wave theory and waves are generated and released into the wave tank. The second relaxation zone is adjacent to the wave generation zone and ensures that the waves propagating in the opposite direction to the generated waves, produced by reflection from the objects placed in the wave tank do not affect the wave generation. This simulates a wave generator with active absorption. The last relaxation zone is the numerical beach, where the values for the free surface and velocity are brought to zero and pressure to its hydrostatic distribution to numerically dissipate the waves from the the wave tank. In this way, the energy in the wave tank is removed by reducing the computational values smoothly without generating waves propagating in the opposite direction.

3. Hydrodynamic Efficiency

The hydrodynamic efficiency of an OWC device is a measure of the wave energy that is available at the turbine for conversion to electrical energy. The power available at the turbine, p_{out} is measured as the time average of the product of the chamber pressure, P_c and the volume flow rate of air across the turbine, q as shown in Eq. 10:

$$p_{out} = \frac{1}{T}\int_0^T P_c(t).\ q(t)dt \tag{10}$$

In the numerical model, the value for the chamber pressure is available at every time step from the solution of the Poisson equation. The volume flow of air is calculated as the product of the velocity of the free surface and the cross-sectional area of the chamber as air is considered to be incompressible in this scenario. This method can be used to analyze the power absorption by the device from incident regular waves.

The incident wave energy flux is calculated using wave theory as shown in Eq. 11

$$p_{in} = \frac{1}{4}\rho g A_0^2 \frac{\omega_i}{k_i}\left(1 + \frac{2k_i d}{sinh\ 2k_i d}\right) \tag{11}$$

where A_0, ω_i, k_i are the amplitude, angular frequency and the wave number of the incident wave respectively and d is the water depth. The equation provides the wave power available per unit width and the wave power available at the mouth of the device is measured by multiplying the width of the device, l. The incident wave power for the fifth-order Stokes waves is calculated using Fenton's theory (Fenton, 1988). Thus, the hydrodynamic efficiency of the device

η is calculated as the ratio of the power available at the turbine to the power incident at the mouth of the device:

$$\eta = \frac{p_{out}}{p_{in}.l} \tag{12}$$

To investigate the performance of the device over different incident wavelengths, the variation of the hydrodynamic efficiency is studied over various values of a dimensionless parameter κd, where $\kappa = \omega_i^2/g$, as in Evans and Porter (1995) and Morris-Thomas et al. (2007)

4. Porous Media Flow Relation

The porous media flow equation is used to represent the external damping provided by a power take-off device on the OWC chamber. A linear pressure drop law is implemented in the model as :

$$\Delta P = -\frac{\mu}{k_p} U_i \tag{13}$$

where μ is the dynamic viscosity of the fluid, ΔP is the pressure drop across the vent and $1/k_p$ is the permeability coefficient. For a given pressure drop, the permeability coefficient can be determined using Darcy's law for flow through porous media:

$$q = \frac{-k_p A}{\mu} \frac{\Delta P}{L} \tag{14}$$

where q is the flow rate, A is the cross-sectional area, and L is the length along the direction of flow.

In a practical scenario, the pressure drop and flow across a turbine is known from the device characteristics supplied by the manufacturer. In this study, the values for the pressure drop and the flow rate across the vent under conditions close to resonance, in the experiments by Morris-Thomas et al. (2007) is used. Using $\Delta P = 500$Pa and $q = 0.11\text{m}^3/\text{s}$, to simulate the pressure drop from a vent of $V = 0.005$m in Eq. 14, results in $1/k_p = 5 \times 10^8 \text{m}^{-2}$. This value of $1/k_p$ is used in all the numerical simulations in this study.

5. Results and Discussion

A grid refinement study is carried out to ensure accurate wave generation and propagation in the numerical wave tank. Linear waves of wavelength $\lambda = 2.90$m and wave height of $H = 0.12$m are generated in the wave tank with a water depth of $d = 0.92$m at grid sizes (dx) of 0.1m, 0.05m, 0.025m and 0.01m. The results are presented in Fig. 1. It is observed that the wave amplitudes are slightly higher at a grid size of $dx = 0.1$m and $dx = 0.05$m. This effect reduces on further refinement of the grid and the wave amplitude converges to the desired value from $dx = 0.025$m. The improvement in the results on refinement from $dx = 0.025$m to $dx = 0.01$m is small. So, a grid size of $dx = 0.025$m can be used for simulations with linear waves. Waves of higher steepness are generated using the fifth-order Stokes wave theory. Grid convergence study is carried out with fifth-order Stokes waves of wavelength $\lambda = 3.53$m and wave height of $H = 0.2$m in a water depth of 0.92m. The results are shown in Fig. 2 and it is seen that the wave amplitudes converge to the desired value from a grid size of $dx = 0.025$m. There is no further improvement in the in the results on decreasing the grid size to $dx = 0.01$m. Thus, a grid size of 0.025m can be used for the simulation of fifth-order Stokes waves. The CFL number is set to 0.1 for all the simulations in this study.

5.1. Validation

In the first set of simulations, the experimental setup in Morris-Thomas et al. (2007) is used as illustrated in Fig. 3. The experiments were conducted at the University of Western Australia on a 1:12.5 scale model of an OWC prototype device. The numerical model is validated by comparing the numerically obtained free surface and pressure to the experimental observations. The OWC device is placed 20m from the wave generation zone in a two-dimensional numerical wave tank of height 2.20m. A grid size of $dx = 0.025$m is used, following the grid convergence study. The wave generation zone is varied according to the incident wavelength in the case and is kept one wavelength long in both in zone 1 and zone 2. The numerical beach behind the device is 1m long. The beach does not have an important effect on the simulation as the device covers the entire width of the tank. The wavelengths used in the experiments with an amplitude $A_0 = 0.06$m are generated in a water depth of $d = 0.92$m. The OWC device has a front wall draught $a = 0.15$m, chamber length $b = 0.64$m, with wall thickness $\delta = 0.04$m and a chamber height of 1.275m. A vent of width $V = 0.05$m is provided and the permeability factor needed to provide the damping from the $V = 0.005$m used in the experiments is determined. The permeability factor required for this is determined to be $1/k_p = 5 \times 10^-8\text{m}^{-2}$ and applied at the vent located at the roof of the device chamber.

A simulation is carried out using linear waves with a wavelength of $\lambda = 4.07$m and amplitude $A_0 = 0.06$m resulting in a wave steepness of $\xi = 0.029$ and $\kappa d = 1.26$. The variation of the free surface $A(t)$ and the chamber pressure, $P_c(t)$ is calculated. The numerical results show a good match with the experimental data for the relative free surface elevation $A(t)/A_0$ and the chamber pressure in Figs. 4a and 4b respectively.

The free surface variation at two points along the center of the model was measured in the experiments and these values used for further analysis. Following the same approach, the free surface elevation is measured in the center of the device chamber in this study in order to replicate the experimental results and to validate the numerical model. The vertical velocity of the free surface w_{fs} is calculated using the time-series data of the free surface variation at the center of the chamber. The velocity of the vertical motion of the free surface in the chamber obtained from the numerical model matches the velocity determined from the experimental data in Fig. 4c. The chamber pressure and the free surface velocity are the two variables that determine the efficiency of the device. The numerical model provides a good representation of these parameters, which is essential for the accurate evaluation of the hydrodynamic efficiency.

Further, simulations are carried out to validate the numerical model for wavelengths on both sides of the resonant wavelength from the experiments. Linear waves of wavelength $\lambda = 7.36$m ($\kappa d = 0.52$) and $\lambda = 2.29$m ($\kappa d = 2.5$)

with an amplitude $A_0 = 0.06$m incident on the device. The numerically obtained values for the motion of the free surface, the pressure and the velocity of the free surface inside the chamber are seen to match the experimental observations in Fig. 5 and Fig. 6 respectively. From the three cases simulated with $\kappa d = 0.52$, 1.26 and 2.5, it is seen that the numerical model provides a good representation of the free surface motion and the pressure in the chamber over a range of wavelengths.

5.2. Effect of Incident Wavelength

Further, simulations with $\kappa d = 0.93, 1.12, 1.52, 1.92$ and 2.93 are carried out with a wave amplitude of $A_0 = 0.06$m. The hydrodynamic efficiency of the device is calculated for each case using Eq. 12 and presented in Fig. 7. The variation of the hydrodynamic efficiency over κd from the numerical model largely agree with the values obtained through experiments by Morris-Thomas et al. (2007) with a peak efficiency of $\eta_{max} = 0.76$ at $\kappa d = 1.26$ slightly higher than the peak efficiency of 0.74 observed in the experiments.

The device efficiency initially increases with increasing κd until it reaches resonance at $\kappa d = 1.26$ and then reduces with further increase in κd. According to Evans and Porter (1995), resonance occurs at $\kappa d = 2$ for small values of b/d and b/a and the fluid motion inside the chamber can be considered similar to the motion of a rigid piston. This uniform motion breaks down with an increase in b/d as the water particles have to travel a longer distance and the resonance occurs at a lower value of κd. In this study, $b/d = 0.7$ and the resonance occurs at $\kappa d = 1.26$ signifying a large difference in the device hydrodynamics at model scale in comparison to the ideal scenario. This can be physically explained using the fluid particle excursions around the device calculated in the simulations. The water particles have a smaller orbital motion under a wave of length $\lambda = 1.96$m ($\kappa d = 2.93$) and a larger orbital motion under a wave of length $\lambda = 4.07$m ($\kappa d = 1.26$). The front wall of the device also interferes more with the shorter particle excursion under a lower wavelength of $\lambda = 1.96$m leading to vortex formation behind the front wall. This leads to a break down of the rigid-piston like motion of the free surface resulting in lower volume flow rate $q(t)$ and a lower device efficiency.

The variation of the free surface relative to the incident amplitude $A(t)/A_0$ has a maximum of $A(t)_{max}/A_0 = 1.0$ and the chamber pressure $P_c = 500$Pa for $\kappa d = 0.52$ in Fig. 5. In the case with maximum efficiency, at $\kappa d = 1.26$, $A(t)_{max}/A_0 = 0.57$ and $P_c = 460$Pa in Fig. 4. In order to understand the lower efficiency of the device under a higher relative oscillation and chamber pressure, the phase of the vertical free surface velocity w_{fs} and the chamber pressure P_c variation for these two cases is studied. The phase difference between P_c and w_{fs} is related to the power absorption by the device as shown in Eq. 15. It arises from the time-average of the product of P_c, w_{fs} and the cross-sectional area of the device which gives a cosine term in the equation:

$$p_{out} = \frac{1}{T}\int_0^T P_c(t).\ q(t)dt = \frac{1}{2}|P_c|.\ |w_{fs}|\ b.l\ cos(\theta) \qquad (15)$$

where θ is the phase difference between P_c and w_{fs}. This equation leads to a reduction in the power absorbed by the device when the variation of P_c and w_{fs} is out of phase. The variation of the vertical velocity of the free surface w_{fs} and the chamber pressure P_c for $\kappa d = 0.52$ is slightly skewed and with a time shift of $0.07T$ or phase difference $\theta = 0.44$rad between w_{fs} and P_c in Fig. 8a. In the case with $\kappa d = 1.26$, w_{fs} and P_c are almost in-phase with a time shift of $0.02T$ or a phase difference of $\theta = 0.125$rad in Fig. 8b. The phase difference can be justified by the fact that the water particle excursions are very large under the longer wavelength at $\kappa d = 0.52$ compared to the particle excursion at $\kappa d = 1.26$. Extending the previously presented argument from Evans and Porter (1995), the large particle excursion leads to significant local particle motion and the free surface motion is no longer uniform along the length of the device for $\kappa d = 0.52$. Consequently, the variation of P_c and w_{fs} for $\kappa d = 0.52$ is irregular compared to the variation for $\kappa d = 1.26$. The phase difference between the variables and the reduced volume flow rate in result in a reduced efficiency at $\kappa d = 0.52$ compared to $\kappa d = 1.26$.

5.3. Effect of Wave Steepness

At first, linear waves with a wave steepness $\xi = H/\lambda = 0.03$ are generated in the numerical wave tank for $\kappa d = 0.52$,0.93, 1.12, 1.26, 1.52, 1.92 and 2.93. The free surface variation inside the device chamber calculated for different incident wavelengths is presented in Fig. 9a. Since the wave steepness of $\xi = 0.03$ is a constant for all the cases simulated here, the longer incident waves have a proportionally higher incident amplitude. It is observed that the amplitude of the free surface motion in the chamber is directly related to the incident amplitude and the highest relative oscillation $A(t)_{max}/A_0$ is seen for $\kappa d = 0.52$ and it is the least for $\kappa d = 2.93$. Incident waves of longer wavelength and amplitude also induce the largest chamber pressure as they carry a higher amount of wave energy. The instantaneous power absorbed $p_{abs} = p_c.\ w_{fs}.\ b$ is calculated for three representative cases, $\kappa d = 0.52$, 1.26 and 2.93. In the case of $\kappa d = 1.26$, the device is close to resonance and almost the same amount of power is absorbed every half wave cycle, seen from the peaks of almost equal amplitude at every 0.5 t/T in Fig. 9b. The instantaneous power absorbed for $\kappa d = 0.52$ and 2.93, which are away from the resonant frequency of the device, are uneven and have lower peaks signifying lower energy absorption in these cases. Under resonant conditions, P_c and q are in phase, resulting in a positive value of power absorbed. This is the power delivered by the device chamber to the turbine that produces electrical energy. In the case of $\kappa d = 2.93$, small parts of the instantaneous power curve cross the positive x-axis in Fig. 9b and result in negative values. This occurs when the chamber pressure and the volume flux are slightly out of phase. The negative values of p_{abs} signify work done by the device to produce outgoing waves due to the phase difference between the chamber pressure and the volume flux.

Next, fifth-order Stokes waves with a wave steepness of $\xi = 0.1$ are generated for $\kappa d = 0.93, 1.26, 1.52, 1.93, 2.49$ and 2.93 to study the hydrodynamic performance of the device under steep non-linear waves. It is not possible to simulate a wave with a steepness of $\xi = 0.1$ with $\kappa d = 0.52$ as the wave amplitude exceeds the height of the device chamber. The relative amplitude motion of the free surface in the chamber $A(t)/A_0$ for a wave steepness of $\xi = 0.1$ is larger for longer waves which have larger amplitudes. This trend is similar to that seen in the case with a wave steepness of $\xi = 0.03$, but the relative amplitudes for all the waves are lower and $A(t)_{max}/A_0 = 0.6$ for $\kappa d = 0.93$ in Fig. 10a. This implies that the steep non-linear waves do not excite the motion of the free surface as much as the waves with lower steepness. The instantaneous power absorbed at $\kappa d = 0.93$, 1.26 and 2.93 in Fig. 10b shows a region where the value for power absorbed is negative, meaning the device spends energy on producing waves radiating away from it. Thus, in spite of a peak of $p_{abs}/p_{in} \approxeq 0.68$, the total power absorbed over a wave period at $\kappa d = 1.26$ is low. In the case of $\kappa d = 0.93$ and 2.93, the peak value of p_{abs}/p_{in} is less than 0.5 and the power absorbed in these two cases is also low. Therefore, the hydrodynamic efficiency of the device in the presence of the steep, non-linear waves is low for all the simulated cases.

The hydrodynamic efficiency of the device is calculated for each of the cases simulated using Eq. 12 and presented in Fig. 11. It is seen that the efficiency curve for $\xi = 0.03$ is similar to the efficiency curve obtained from the previous simulations with a constant incident amplitude of $A_0 = 0.06$m. This shows that the wave steepness does not have a large influence on the device efficiency when linear waves of low steepness are incident. Whereas in the case of non-linear waves of steepness $\xi = 0.1$, the device efficiency is reduced considerably and is of the order $\eta \approxeq 0.35$. This is in agreement with the analysis of the variation of the free surface, chamber pressure and the instantaneous power absorption above.

The motion of the water particles in front of the device and the variation of the free surface in the chamber is further investigated at the resonant condition, $\kappa d = 1.26$, to obtain a better understanding of the difference in efficiency of the device for waves of different steepnesses. The streamlines in front of the device are studied over the duration of a wave period, along with the free surface motion inside the chamber of the device, during which the device completes one cycle of exhalation and inhalation of air through the vent in the roof of the chamber.

Figure 12 shows the motion of the free surface in the chamber and the streamlines around the device for $\kappa d = 1.26$ at a wave steepness of $\xi = 0.03$. In Fig. 12a, the process of inhalation has just been completed and the free surface is correspondingly at its lowest elevation. The process of exhalation of air begins in Fig. 12b and the free surface is seen uniformly moving upwards. A recirculation zone starts to form behind the front wall as the water moves into the chamber (Fig. 12c) and moves towards the back wall and is then dissipated. The motion of the free surface is at its maximum in Fig. 12d at the end of the exhalation phase and the water column is horizontal due to the rigid piston-like motion of the water column at resonance. The inhalation phase is seen in Figs. 12e and 12f and the free surface moves downwards uniformly. There is no major disturbance of the water column or the free surface as the chamber inhales air through the vent in the roof. The recirculation zones seen in Fig.12c behind the front wall and near the bottom at the back wall in Fig.12d disintegrate in a very short time, under 0.04 t/T and the loss of wave energy due to flow separation behind the front wall and recirculation at the bottom of the chamber can be said to be low. Thus, $\kappa d = 1.26$ produces a resonant, rigid piston-like motion in the chamber of the device and most of the incident wave energy is delivered at the vent for conversion into electrical energy by the turbine. The free surface just outside the chamber is almost horizontal indicating that the device absorbs most of the incident waves and wave reflection from the device is low.

The behavior of the OWC device over one wave period, when fifth-order Stokes waves with $\kappa d = 1.26$ and a steepness of $\xi = 0.1$ are incident on it is seen in Fig. 13. The device has just completed the inhalation phase in Fig. 13a and the free surface is at its lowest elevation and a crest is approaching the device. The approaching crest is seen to build up against the front wall of the device in Fig. 13b even as the device just begins its exhalation phase. The formation of recirculation zones is seen behind the front wall in Figs. 13c and 13d and is more prominent than in the case with $\xi = 0.1$. The vortices are also seen to form in front of the back wall towards the bottom of the device in Figs. 13e and

13f. The water elevation outside the chamber is at a minimum in Figs. 13f and 13g, when the device has started its inhalation phase and is in the process of pushing the water out of the chamber. This shows that the motion of the water around the device and the motion inside the device chamber are very much out of phase and the device is not absorbing all the incident wave energy. The free surface is not uniform in this case and there is a break down of the resonance that is seen at the same value of κd with $\xi = 0.03$. The motion of the water column is less uniform with the formation of eddies and prominent recirculation zones inside the chamber, behind the front wall and in front of the back wall towards the bottom of the chamber. The disturbance in the flow due to the flow separation behind the front wall and the recirculation zone at the bottom of the chamber near the back wall is sustained for a longer period of time, about 0.44 t/T in this case, compared to when $\xi = 0.03$. This sustained disturbance in the flow is one of the contributors to the larger phase difference between the variation of the chamber pressure and the motion of the water column seen in this case. The energy lost due to the vortex formation and the larger phase difference between the chamber pressure and the volume flux of air through the chamber results in a lower power absorption by the device. Thus, the efficiency of the device with $\kappa d = 1.26$ at a higher wave steepness of $\xi = 0.1$ is low.

6. Conclusion

A CFD based two-dimensional numerical wave tank was used to study the hydrodynamics of an OWC device with incident regular waves. The numerical model was validated by comparing the variation of the free surface, the pressure and the vertical velocity of the free surface inside the device chamber for different wavelengths. The numerical results agreed well with the experimental data and the model produced a realistic representation of the flow physics involved. The pressure drop on the device chamber from a PTO device was modeled using the porous media flow theory. The permeability constant required was determined using the experimental data.

The variation of the hydrodynamic efficiency with the incident wavelength was studied. The occurrence of resonance at lower values of the relative depth κd for values of b/d closer to 1 than in the ideal scenario with $b/d \ll 1$ is discussed. The longer particle excursion required at higher values of b/d and the higher influence of the front wall on the particle excursion cause a break down of the rigid piston-like motion of the free surface inside the device chamber at wavelengths away from resonance. The variation of the pressure and free surface inside the chamber at various incident wavelengths was studied. The phase difference between the variation of the chamber pressure and the vertical velocity of the free surface resulting from local motion of the free surface contributed to the lowering of the device efficiency, inspite of large oscillations of the free surface and chamber pressure.

Simulations using linear waves of wave steepnesses $\xi = 0.03$ and non-linear waves of wave steepness $\xi = 0.1$ were carried out to study the influence of wave steepness and non-linear waves on the hydrodynamics of the device. The efficiency curve for $\xi = 0.03$ was found to be similar to the curve obtained from experiments and simulations using a range of wavelengths of linear waves with a constant amplitude of 0.06m. On the the other hand, the efficiency of the device was very poor, when exposed to fifth-order Stokes waves of a higher wave steepness. The wavelength, which produced resonant response at a steepness of $\xi = 0.03$, did not produce resonance in the device at a steepness of $\xi = 0.1$. The free surface motion and streamlines around the device at $\kappa d = 1.26$ for steepnesses $\xi = 0.03$ and $\xi = 0.1$ were studied and rigid piston-like motion was seen in the simulation with the lower wave steepness. The motion of the free surface was non-uniform at the higher wave steepness of $\xi = 0.1$. Thus, in addition to the wavelength of the incident waves, the wave steepness also has a significance impact on the hydrodynamic efficiency of an OWC device.

The numerical model provides a large amount of information regarding the flow physics in and around an OWC device and the behavior of the device under various conditions of incident waves and geometric configurations can be investigated using the chamber pressure and the motion of the free surface. The external damping is defined explicitly using the porous media theory and can be used to explore phase control methods to improve the performance of the device by controlling the damping on the device chamber. Further studies can be carried out to investigate the use of phase control to improve the device efficiency, formation, propagation and dissipation of vortices in the device chamber, and their influence on the hydrodynamic efficiency and also evaluate the wave forces acting on the device in order to design efficient and stable OWC devices for commercial deployment.

Acknowledgements

The authors are thankful to Michael Morris-Thomas, Principal Naval Architect, Worley Parsons, Perth, Australia for the experimental data and helpful discussions. This study has been carried out under the OWCBW project (No. 217622/E20) and the authors are grateful to the grants provided by the Research Council of Norway. This study was supported in part with computational resources at the Norwegian University of Science and Technology (NTNU) provided by NOTUR, http://www.notur.no.

Berthelsen, P.A., Faltinsen, O.M., 2008. A local directional ghost cell approach for incompressible viscous flow problems with irregular boundaries. Journal of Computational Physics 227, 4354–4397.

Bradshaw, P., Ferriss, D.H., Atwell, N.P., 1967. Calculation of boundary layer development using the turbulent energy equation. Journal of Fluid Mechanics 28, 593–616.

Chorin, A., 1968. Numerical solution of the Navier-Stokes equations. Mathematics of Computation 22, 745–762.

Didier, E., Paixão Conde, J.M., Teixeira, P.R.F., 2011. Numerical simulation of an oscillating water column wave energy convertor with and without damping, in: Proc., International Conference on Computational Methods in Marine Engineering.

Durbin, P.A., 2009. Limiters and wall treatments in applied turbulence modeling. Fluid Dynamics Research 41, 1–18.

Egorov, Y., 2004. Validation of CFD codes with PTS-relevant test cases. Technical Report 5th Euratom framework programme ECORA project, EVOL-ECORA D07.

Engsig-Karup, A.P., 2006. Unstructured nodal DG-FEM solution of high-order boussinesq-type equations. Ph.D. thesis. Technical University of Denmark, Lyngby.

Evans, D.V., 1978. Oscillating water column wave energy convertors. IMA Journal of Applied Mathematics 22, 423–433.

Evans, D.V., 1982. Wave power absorption by systems of oscillating surface pressure distributions. Journal of Fluid Mechanics 114, 481–499.

Evans, D.V., Porter, R., 1995. Hydrodynamic characteristics of an oscillating water column device. Applied Ocean Research 17, 155–164.

Falcão, A.F.O., Henriques, J.C.C., 2014. Model prototype similarity of oscillating-water-column wave energy converters. International Journal of Marine Energy 6, 18–34.

Falcão, A.F.O., Justino, P.A.P., 1999. OWC wave energy devices with air flow control. Ocean Engineering 26, 1275–1295.

Fenton, J.D., 1988. The numerical solution of steady water wave problems. Computers and Geosciences 14, 357–368.

Hoskin, R.E., Count, B.M., Nichols, N.K., Nicol, D.A.C., 1986. Phase control for the oscillating water column, in: Evans, D.V., Falcão, A.F.O. (Eds.), Hydrodynamics of Ocean Wave-Energy Utilization. Springer Berlin Heidelberg, pp. 257–268.

Jacobsen, N.G., Fuhrman, D.R., Fredsøe, J., 2011. A wave generation toolbox for the open-source CFD library: OpenFOAM. International Journal for Numerical Methods in Fluids 70, 1073–1088.

Jiang, G.S., Peng, D., 2000. Weighted eno schemes for Hamilton-Jacobi equations. SIAM Journal on Scientific Computing 21, 2126–2143.

Jiang, G.S., Shu, C.W., 1996. Efficient implementation of weighted ENO schemes. Journal of Computational Physics 126, 202–228.

Lopes, M.F.P., Hals, J., Gomes, R.P.F., Moan, T., Gato, L.M.C., Falcão, A.F.O., 2009. Experimental and numerical investigation of non-predictive phase-control strategies for a point-absorbing wave energy converter. Ocean Engineering 36, 386 – 402.

López, I., Pereiras, B., Castro, F., Iglesias, G., 2014. Optimisation of turbine-induced damping for an OWC wave energy converter using a RANS-VOF numerical model. Applied Energy 127, 105–114.

Mayer, S., Garapon, A., Sørensen, L.S., 1998. A fractional step method for unsteady free surface flow with applications to non-linear wave dynamics. International Journal for Numerical Methods in Fluids 28, 293–315.

Morris-Thomas, M.T., Irvin, R.J., Thiagarajan, K.P., 2007. An investigation into the hydrodynamic efficiency of an oscillating water column. Journal of Offshore Mechanics and Arctic Engineering 129, 273–278.

Peng, D., Merriman, B., Osher, S., Zhao, H., Kang, M., 1999. A PDE-based fast local level set method. Journal of Computational Physics 155, 410–438.

Sarmento, A.J.N.A., 1992. Wave flume experiments on two-dimensional oscillating water column wave energy devices. Experiments in Fluids 12, 286–292.

Sarmento, A.J.N.A., Falcão, A.F.O., 1985. Wave generation by an oscillating surface pressure and its application in wave energy extraction. Journal of Fluid Mechanics 150, 467–485.

Shu, C.W., Osher, S., 1988. Efficient implementation of essentially non-oscillatory shock capturing schemes. Journal of Computational Physics 77, 439–471.

Teixeira, P.R.F., Davyt, D.P., Didier, E., Ramalhais, R., 2013. Numerical simulation of an oscillating water column device using a code based on Navier-Stokes equations. Energy 61, 513–530.

Thiruvenkatasamy, K., Neelamani, S., 1997. On the efficiency of wave energy caissons in array. Applied Ocean Research 19, 61–72.

van der Vorst, H., 1992. BiCGStab: A fast and smoothly converging variant of Bi-CG for the solution of nonsymmetric linear systems. SIAM Journal on Scientific and Statistical Computing 13, 631–644.

Wilcox, D.C., 1994. Turbulence modeling for CFD. DCW Industries Inc., La Canada, California.

Zhang, Y., Zou, Q.P., Greaves, D., 2012. Air-water two phase flow modelling of hydrodynamic performance of an oscillating water column device. Renewable Energy 41, 159–170.

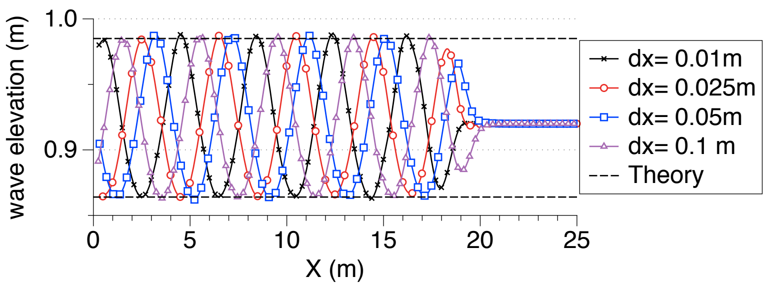

Figure 1: Grid Convergence for linear waves

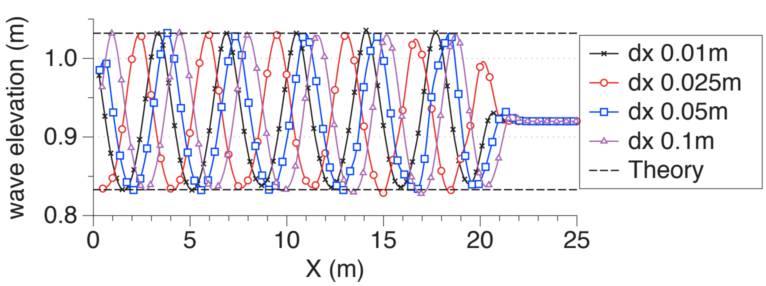

Figure 2: Grid Convergence for $5th$-order Stokes waves

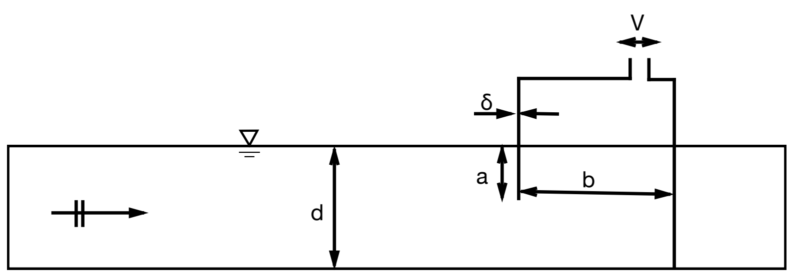

Figure 3: Schematic of the OWC device used in the simulations

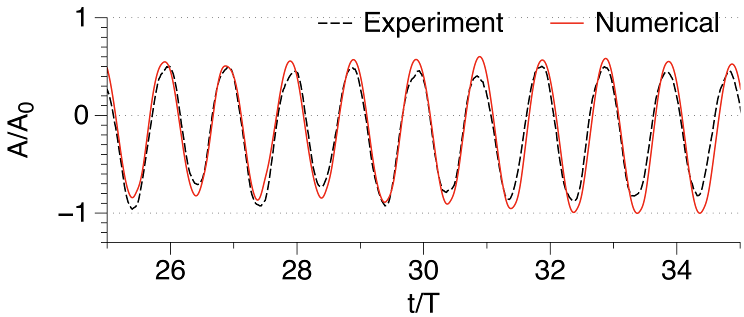

(a) relative free surface elevation at the centre of the chamber

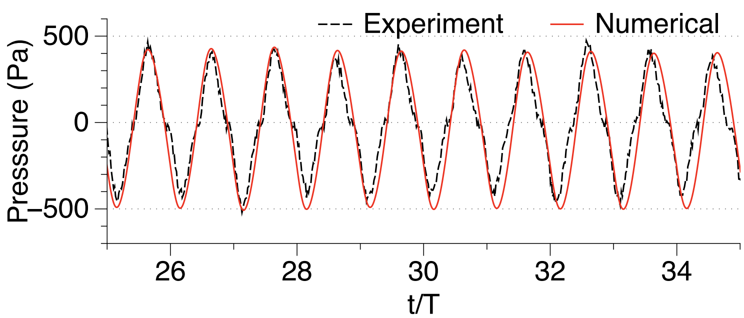

(b) variation of chamber pressure

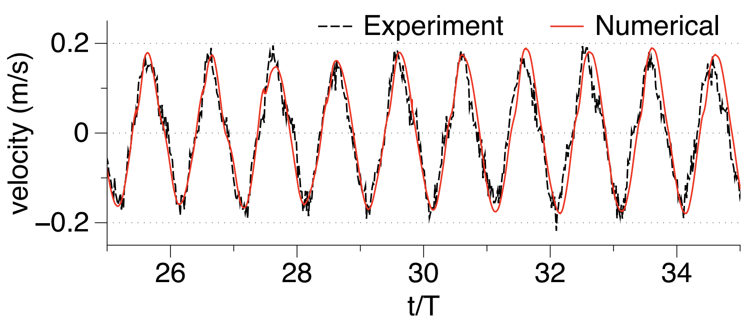

(c) velocity of the free surface

Figure 4: Comparison of relative free surface elevation, velocity of the free surface and pressure inside the chamber for $\kappa d = 1.26$ and $\xi = 0.029$

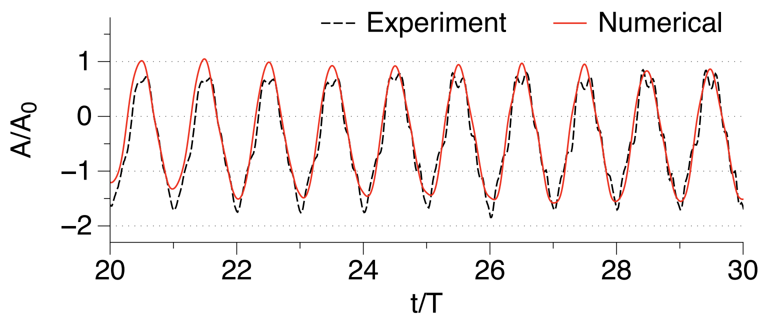

(a) relative free surface elevation at the centre of the chamber

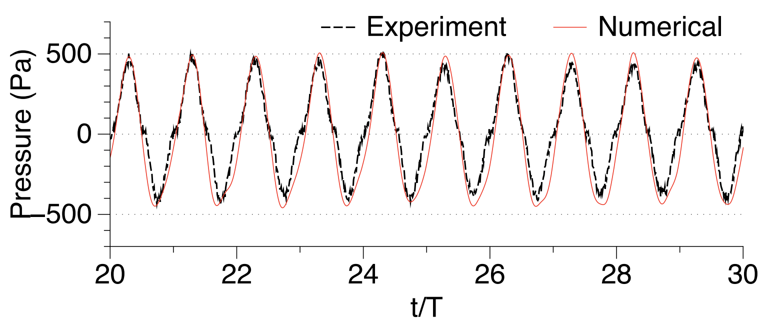

(b) variation of chamber pressure

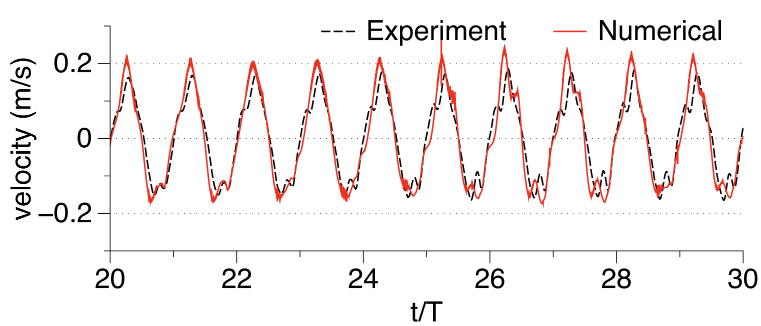

(c) velocity of the free surface

Figure 5: Comparison of relative free surface elevation, velocity of the free surface and pressure inside the chamber for $\kappa d = 0.52$ and $\xi = 0.016$

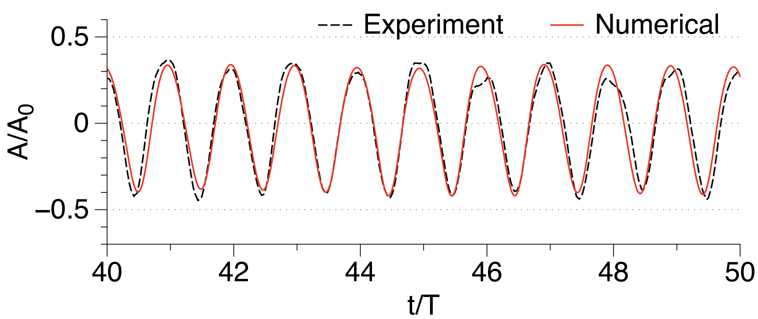

(a) relative free surface elevation at the centre of the chamber

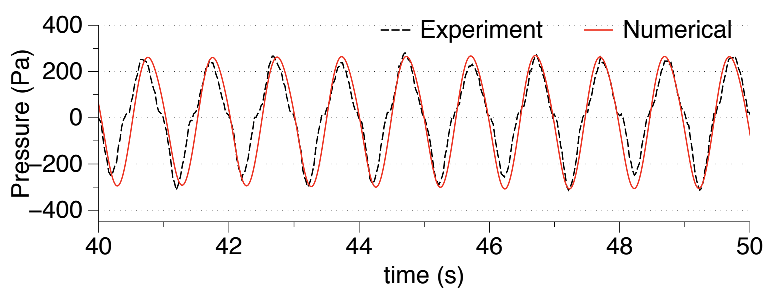

(b) variation of chamber pressure

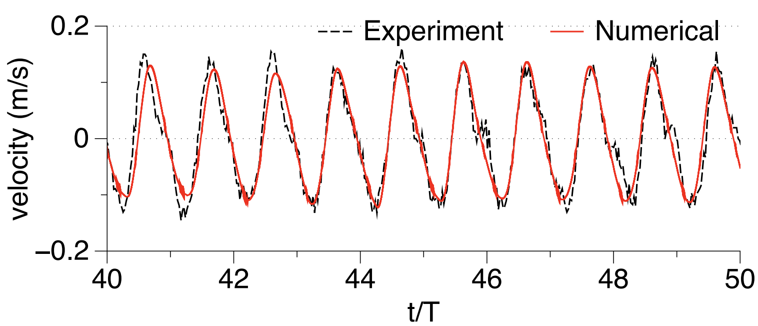

(c) velocity of the free surface

Figure 6: Comparison of relative free surface elevation, velocity of the free surface and pressure inside the chamber for $\kappa d = 2.5$ and $\xi = 0.052$

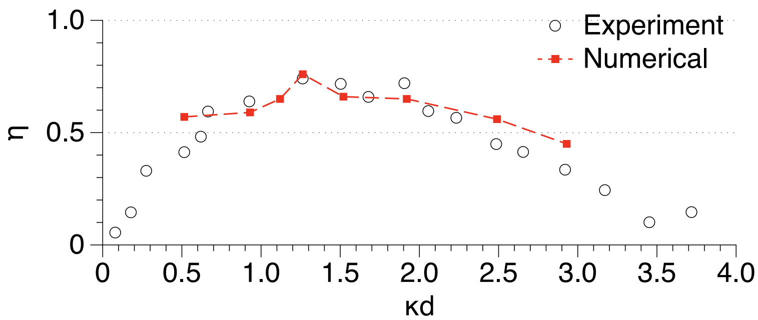

Figure 7: Hydrodynamic efficiency of the device vs. κd

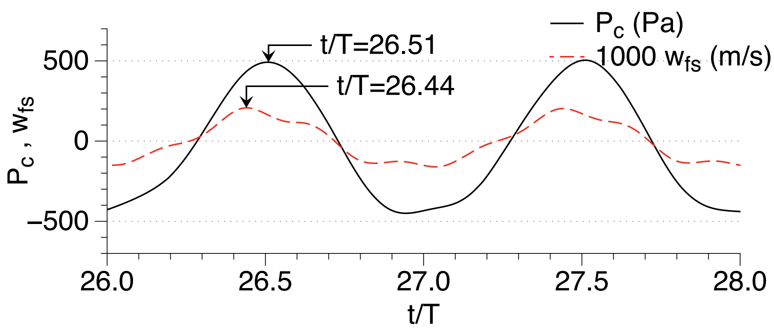

(a) variation of P_c and w_{fs} for $\kappa d = 0.52$

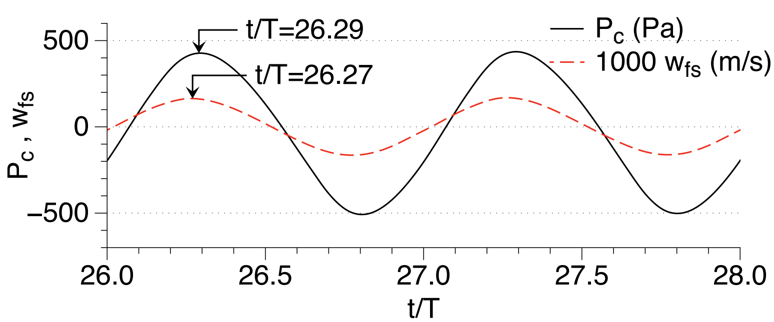

(b) variation of P_c and w_{fs} for $\kappa d = 1.26$

Figure 8: Comparison of phase difference between vertical free surface velocity and chamber pressure for $\kappa d = 0.52$ and 1.26

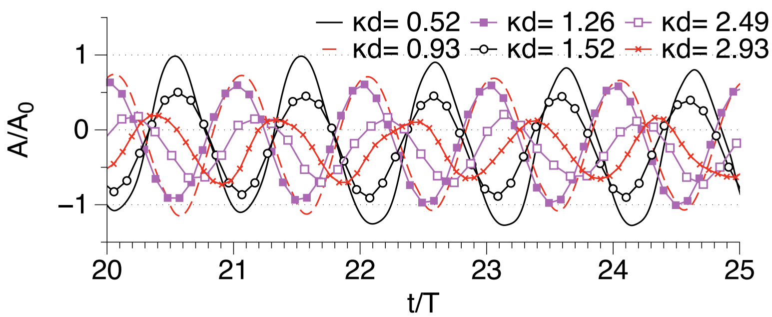

(a) variation of the relative free surface at the center of the chamber

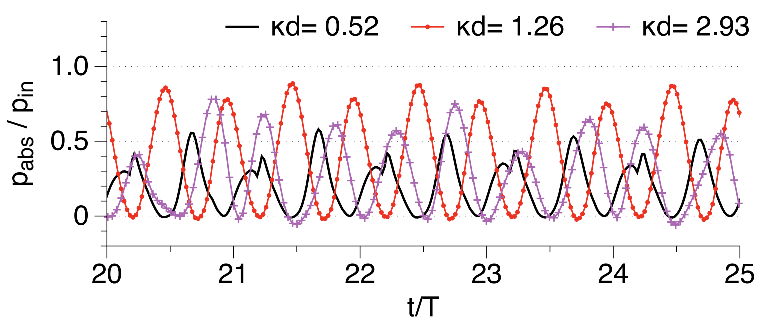

(b) Instantaneous power absorption ratio for $\kappa d = 0.52, 1.26$ and 2.93 at $\xi = 0.03$

Figure 9: Variation of free surface in the device chamber and instantaneous power absorbed for different κd at $\xi = 0.03$

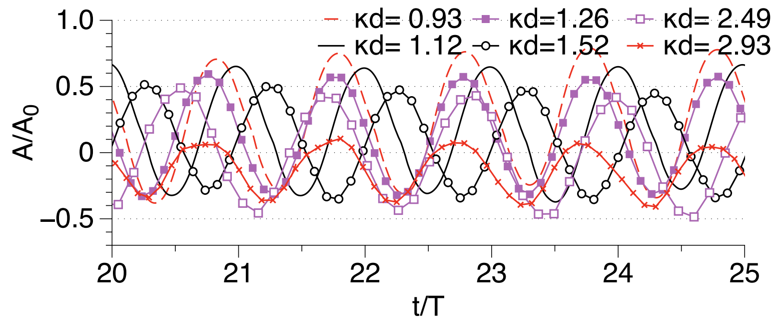

(a) variation of the relative free surface at the center of the chamber

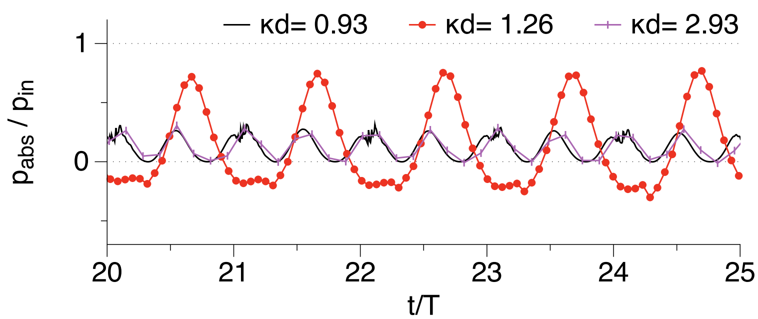

(b) Instantaneous power absorption ratio for $\kappa d = 0.93, 1.26$ and 2.93 at $\xi = 0.1$ using $5th$-order Stokes waves

Figure 10: Variation of free surface in the device chamber and instantaneous power absorbed for different κd at $\xi = 0.1$ using $5th$-order Stokes waves

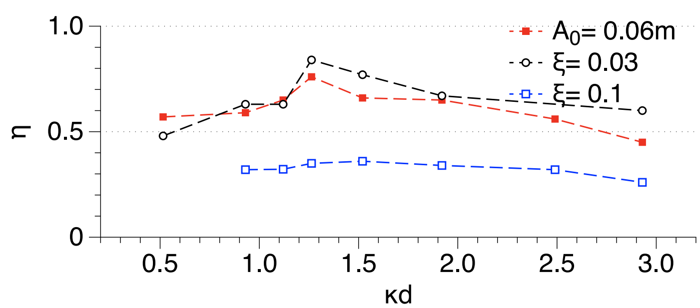

Figure 11: Hydrodynamic efficiency of the device vs. κd for $\xi = 0.03$, $\xi = 0.1$ and $A_0 = 0.06\text{m}$

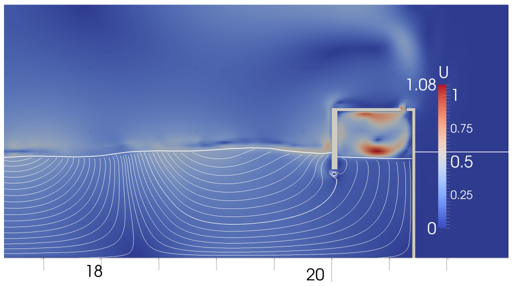

(a) $t/T = 59.57$

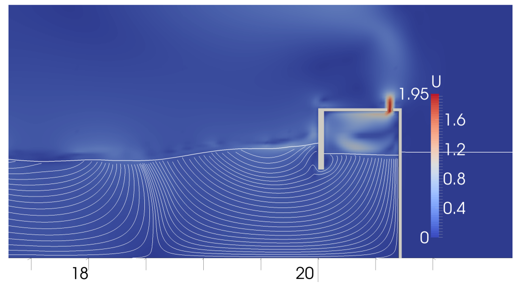

(b) $t/T = 59.72$

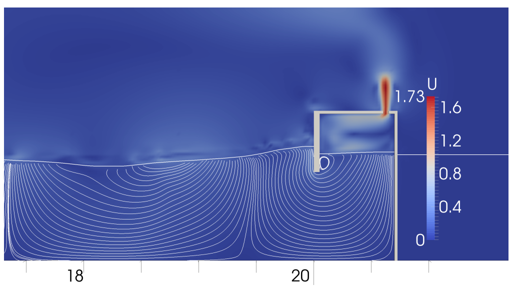

(c) $t/T = 59.86$

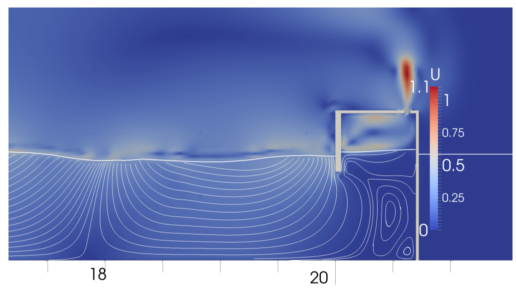

(d) $t/T = 60.01$

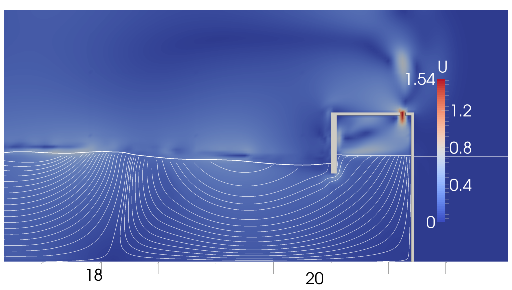

(e) $t/T = 60.15$

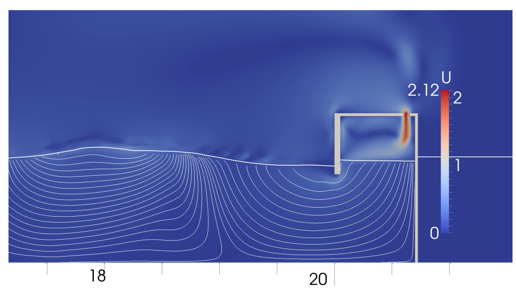

(f) $t/T = 60.30$

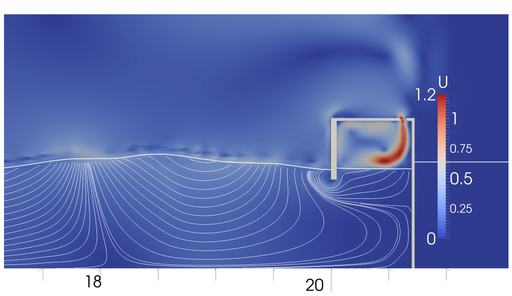

(g) $t/T = 60.44$

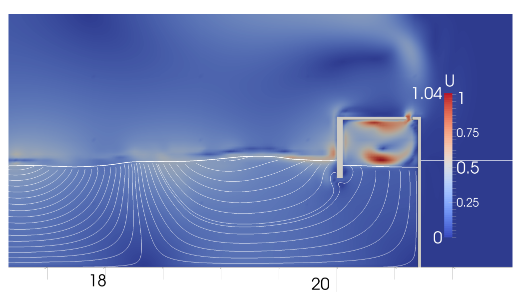

(h) $t/T = 60.59$

Figure 12: Streamlines in front of the device and free surface in the chamber for $\kappa d = 1.26$ at $\xi = 0.03$ over half a wave period

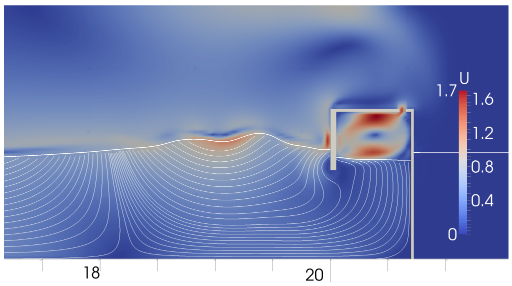

(a) $t/T = 21.32$

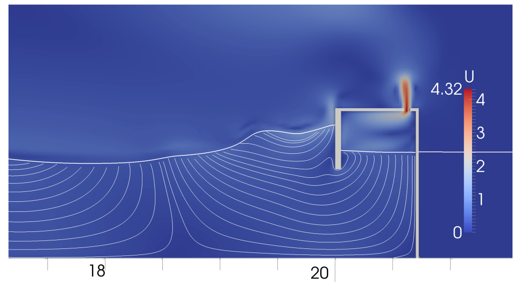

(b) $t/T = 21.46$

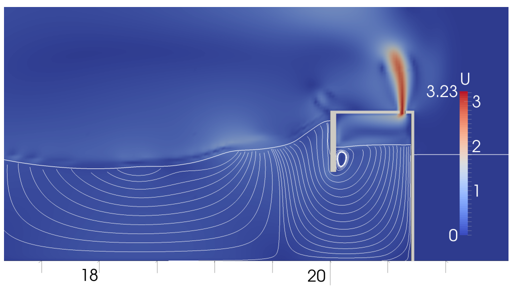

(c) $t/T = 21.61$

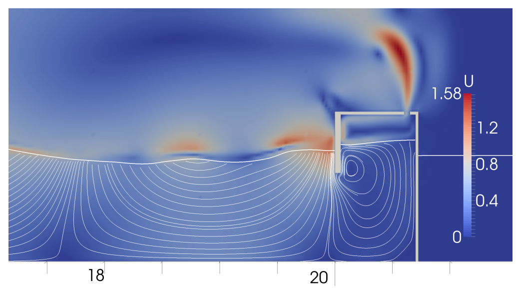

(d) $t/T = 21.76$

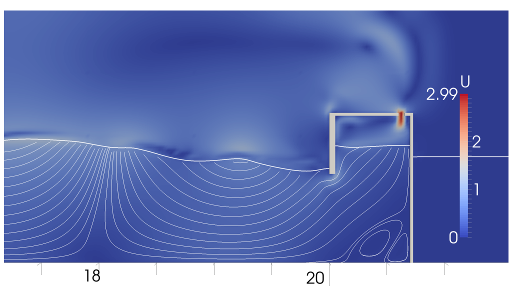

(e) $t/T = 21.90$

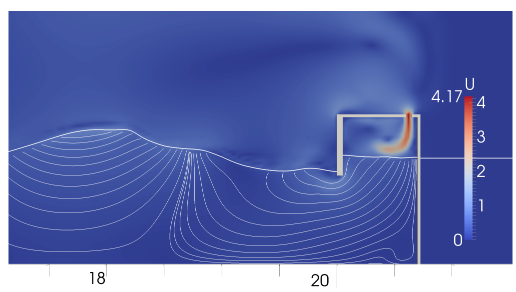

(f) $t/T = 22.05$

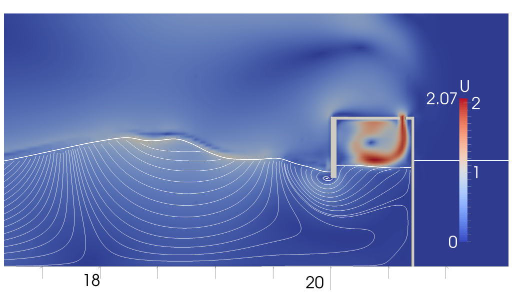

(g) $t/T = 22.19$

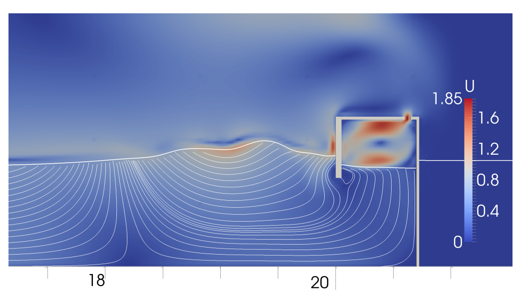

(h) $t/T = 22.34$

Figure 13: Streamlines in front of the device and free surface in the chamber for $\kappa d = 1.26$ at $\xi = 0.1$ over the duration of a wave period